Received September 5, 2021, accepted October 2, 2021, date of publication October 26, 2021, date of current version November 3, 2021.

Digital Object Identifier 10.1109/ACCESS.2021.3121292

In-Depth Study of 3D Color-Resist Coating Process for Optically Uniform Image Sensors

SUNGJUN KIM[1,2,3], (Member, IEEE), JAESANG YOO[1], HAKYU CHOI[1], JAEKWAN SEO[1], SUNGHUN LEE[4], SANG MIN WON[4], JIN-HONG PARK[4], (Member, IEEE), AND KEUN HEO[5], (Member, IEEE)

[1]Foundry Business, Samsung Electronics Company, Kyunggi-do 446-711, South Korea
[2]Samsung Institute of Technology, Kyunggi-do 446-711, South Korea
[3]Department of Semiconductor and Display Engineering, Sungkyunkwan University, Suwon-si, Kyunggi-do 16419, South Korea
[4]Department of Electrical and Computer Engineering, Sungkyunkwan University, Suwon-si, Kyunggi-do 16419, South Korea
[5]School of Semiconductor and Chemical Engineering, Semiconductor Physics Research Center, Jeonbuk National University, Jeonju-si, Jeollabuk-do 54896, South Korea

Corresponding authors: Jin-Hong Park (jhpark9@skku.edu) and Keun Heo (kheo@jbnu.ac.kr)

This work was supported in part by the Ministry of Small and Medium Enterprises (SMEs) and Startups under Grant S3115652; in part by the Research Funds for Newly Appointed Professors of Jeonbuk National University, in 2021; and in part by the NRF Grant funded by the Korea Government Ministry of Science, ICT & Future Planning under Grant NRF-2021R1C1C1009410 and Grant IITP-2020-0-01821.

ABSTRACT The color filter required for manufacturing a CMOS image sensor was redeveloped to optimize its optical uniformity. An in-depth study of the three-dimensional (3D) coating process and how it gives rise to various radial-shaped striation patterns was conducted. These radial-shaped striation patterns were systematically investigated with reference to two types of patterns: the orthogonal type found only at the orthogonal edges of the wafer and the diagonal type found mostly at the corner of each quadrant. The formation of the orthogonal pattern was based on the wide standing wave created by the incident force of the spreading color photoresist (PR) and the reflective force from the bump pads acting as coating barriers. The diagonal pattern was found to be generated by the turbulent wakes created behind the bump pads by the drag force, which interfered with the coating flow. An in-depth study using Ansys CFX software and an in-line inspection tool revealed that lowering the viscosity of the color PR material is a key factor for improving the phenomenon whereby the 3D striation patterns of the orthogonal and diagonal types are formed. Based on this finding, it was possible to drastically reduce the formation of the 3D striation patterns by decreasing the viscosity of the material comprising each color PR. This study provides not only an empirical and theoretical understanding of the 3D color PR coating mechanism, but also guidelines for future color filter processes.

INDEX TERMS CMOS image sensor, color filter process, spin coating, radial striation pattern, fluidic dynamics, process optimization.

I. INTRODUCTION

Since the advent of the mobile era, the CMOS image sensor (CIS) market has grown drastically owing to the strong demand for high-quality images captured by portable device cameras [1], [2]. Although recent advances in resolution and shooting speed has improved the quality of the image, noise in the form of faint patterns (e.g., discoloring and staining) due to the inherent factors in the manufacturing process of CIS are still technical challenge [3], [4]. Here, a color filter (CF) is a key component for obtaining spectral color information from light, maintaining optical uniformity, and suppressing optical noise in CISs [5]. Many CF fabrication methods, such as dyeing [6], [7], pigment dispersion [8], [9], printing [10], [11], and electrodeposition [12], [13] have been proposed. Among them, the pigment dispersion process has been the most widely used in the industry to form CFs owing to its superior color reproducibility and fine resolution with a wide process margin and excellent scalability for mass production [14]. However, variation in the pigment size and uneven pigment dispersion are limitation for the physical and optical uniformity of a CF film fabricated with

The associate editor coordinating the review of this manuscript and approving it for publication was Taous Meriem Laleg-Kirati.

This work is licensed under a Creative Commons Attribution 4.0 License. For more information, see https://creativecommons.org/licenses/by/4.0/

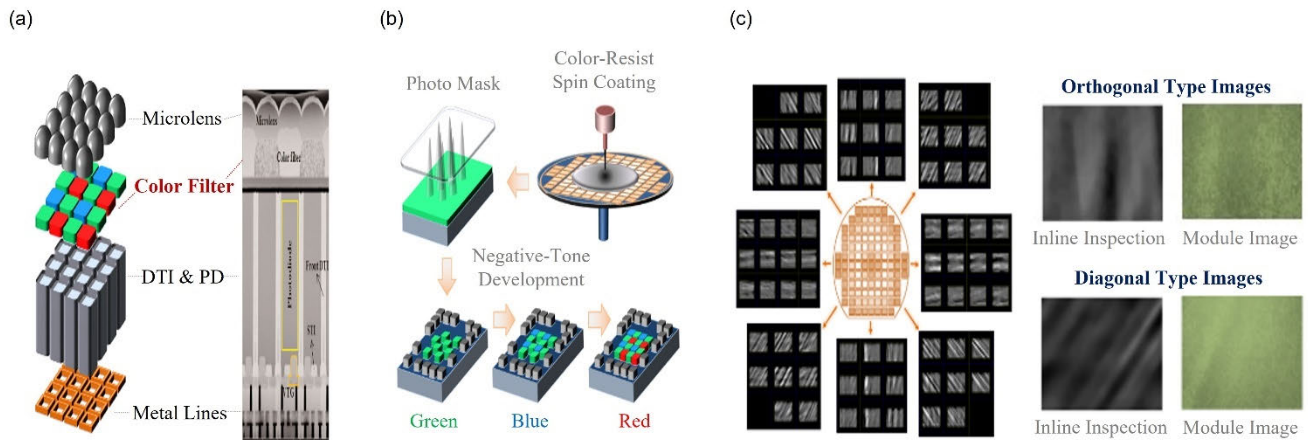

FIGURE 1. Graphical description of color PR patterning process and radial striation pattern phenomenon: (a) an image sensor pixel array structure including micro-lens for light collection, a color filter for light separation, deep trench isolation (DTI) for blocking crosstalk, and a photodiode (PD) for light conversion; (b) color filter patterning process, showing the color PR coating order; and (c) inspection results after unoptimized color PR coating process for investigating the radial direction of the striation phenomenon on the PR, categorized as orthogonal and diagonal types.

the pigment-type process [15]. In addition, the pigment-type coating process on the bump pads and the surface groove by the preceding integration during the CIS manufacturing process make it more difficult to ensure the uniformity of the optical properties.

In recent years, state-of-the-art research has been conducted to overcome these physical limitations and improve the optical properties of CF arrays by (1) employing the advanced CF remosaic method, (2) improving the optical stack structure, and (3) using a novel coating method for increased thickness uniformity.

Jang *et al.* achieved excellent color sensitivity and signal-to-noise ratio (SNR) by using Tetra- and Nona-mode remosaic schemes, even under low illumination conditions [16], [17]. Park *et al.* and Joe *et al.* improved the sensitivity and Y-SNR by adopting a low-reflection material as the CF isolation grid in a buried CF structure [18], [19]. Huang *et al.* and Yan *et al.* fabricated a highly planarized coating film through a two-step spin-coating process [20] and spin-coating process with a vacuum treatment technique [21] on topographical substrates. Although these studies succeeded in realizing superior color properties, the direct application of these new technologies to industry carries significant burdens due to the (1) design overhead (2) fabrication costs, and (3) process complexity. Accordingly, based on the existing spin-coating process, detailed studies for improving the optical properties—to make them comparable to the aforementioned state-of-the-art CFs—have not yet been conducted.

Herein, we present a CF manufacturing process to achieve optical uniformity, which we developed by conducting an in-depth study of the 3D coating process. The radial-shaped 3D striation patterns were systematically investigated in terms of the variations in the color-resist coating process. A computational fluid dynamics (CFD) tool, Ansys CFX software [22], and an in-line inspection metrology tool were used to thoroughly analyze the phenomenon responsible for the formation of the 3D striation pattern. Subsequently, the key parameters for controlling the variation in the film thickness were derived. The 3D striation patterns were drastically improved by adjusting the key parameters and optimizing the 3D color photoresist (PR) process.

II. COLOR PR PATTERNING PROCESS AND RADIAL STRIATION PATTERN PHENOMENON

The structure of the conventional CIS array is illustrated in Fig. 1(a) [1]. One image sensor array unit consists of a photodiode (PD) for converting the light into a signal, deep trench isolation to reduce crosstalk between pixels, a CF for separating natural light into its green, red, and blue components, and a micro-lens to improve light collection. The fabrication process of the CF array should be carefully managed to ensure excellent color purity and transmittance. Fig. 1(b) illustrates the relevant CF patterning process. The color PR is a negative-tone photosensitive material from which areas exposed to UV light are removed after development [14]. Contrary to the conventional photo/etching process, the color PR remains permanent after processing and acts as an optical filter. Therefore, it is crucial to manage process variations in the thickness, critical dimension (CD), and species concentration to improve the optical uniformity. Fig. 1(c) shows the inspection results after the unoptimized color PR coating process. The radial-direction striation phenomenon on the coated PR was investigated and categorized into orthogonal and diagonal types. Orthogonal patterns were found only at the 12, 3, 6, and 9 o'clock edges on the wafer, whereas diagonal patterns were found at each diagonal edge. The strip patterns measured by the in-line inspection tool matched the images captured in the module condition well. These results indicated that the CF coating process would have to be optimized to obtain extremely high optical integrity.

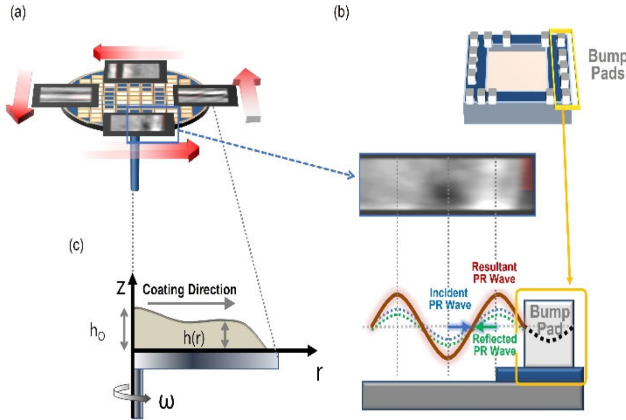

FIGURE 2. Graphical description of orthogonal striation pattern: (a) orthogonal pattern generation during spin-coating process, (b) standing wave generation from the bump pad wall side, (c) illustration of the color PR spreading process on the substrate with polar cylindrical coordinates.

III. INVESTIGATION OF THE ORTHOGONAL STRIATION PATTERN

The mechanism underlying the formation of the orthogonal pattern is explained by graphically depicting the spreading process of the color PR in Fig. 2(a). During the coating process, the color PR is spread by the Coriolis force [23]. Thus, the color PR experiences a maximum force in the spinning direction toward the wafer edge. On each edge of the wafer, at 12, 3, 6, and 9 o'clock, the PR hits the bump pads along the orthogonal direction, where the reflective force from the pads is maximized, generating huge standing waves in the orthogonal direction, as shown in Fig. 2(b). The forces influencing the spin-coating process were further investigated to determine the critical parameters for controlling the variation in the CF film thickness. We only considered the Navier–Stokes equation (Equation (1)) in the radial direction with cylindrical polar coordinates (r, θ, z), as shown in Fig. 2(c) [24].

$$\rho\left(\frac{\partial \upsilon_r}{\partial t}+\upsilon_r\frac{\partial \upsilon_r}{\partial r}+\frac{\upsilon_\theta}{r}\frac{\partial \upsilon_r}{\partial \theta}-\frac{\upsilon_\theta^2}{r}+\upsilon_z\frac{\partial \upsilon_r}{\partial z}\right)$$
$$=-\frac{\partial P}{\partial r}+\rho g_r+\mu\left[\frac{\partial}{\partial r}\left(\frac{1}{r}\frac{\partial}{\partial r}(r\upsilon_r)\right)+\frac{1}{r^2}\frac{\partial^2\upsilon_r}{\partial\theta^2}-\frac{2}{r^2}\frac{\partial\upsilon_\theta}{\partial\theta}+\frac{\partial \upsilon_r^2}{\partial z^2}\right], \quad (1)$$

where ρ is the density of the fluid, P is the equivalent pressure, g_r is the gravitational acceleration in the r direction, and μ is the viscosity of the material. The fluid velocity components in each direction are expressed as υ_{r}, υ_θ, and υ_z, respectively. For simplicity, the following assumptions were made: (i) the flow of color PR is assumed to be in a steady state ($\partial\upsilon_r/\partial t = 0$). ($ii$) The spread of color PR is assumed to be radially symmetric ($\partial\upsilon_r/\partial\theta = 0$, $\partial^2\upsilon_r/\partial\theta^2 = 0$) and to rotate with the substrate ($\partial\upsilon_\theta/\partial\theta = 0$). ($iii$) There is no radial gravitational component because the rotating wafer is horizontal ($g_r = 0$). The velocity component in the z-direction perpendicular to the rotating wafer was also negligible because the film was very thin ($\upsilon_z = 0$). The color PR is assumed to be an incompressible Newtonian fluid with a constant mass density and viscosity, independent of the shear rate. (vi) Evaporation of the color PR is negligible. Based on the aforementioned assumptions, the Navier–Stokes equation (Equation (1)) for the color PR coating process can be simplified to Equation (2) by substituting $\upsilon_\theta = r\omega$, where ω is the angular velocity.

$$\rho\left(\upsilon_r\frac{\partial\upsilon_r}{\partial r}-r\omega^2\right)=-\frac{\partial\rho}{\partial r}+\mu\left[\frac{1}{r}\frac{\partial}{\partial r}\left(r\frac{\partial\upsilon_r}{\partial r}\right)+\frac{\partial\upsilon_r^2}{\partial z^2}-\frac{\upsilon_r}{r^2}\right] \quad (2)$$

We introduced a rescaled coordinate $r* = \varepsilon r$, assuming that the height of the color PR is significantly less than its radius, where ε is a very small dimensionless number. Equation (2) can then be simplified as Equation (3).

$$\rho\left(\varepsilon\upsilon_r\frac{\partial\upsilon_r}{\partial r^*}-\frac{r^*\omega^2}{\varepsilon}\right)=-\varepsilon\frac{\partial\rho}{\partial r^*}+\mu\left[\varepsilon^2\frac{1}{r^*}\frac{\partial}{\partial r^*}\left(r^*\frac{\partial\upsilon_r}{\partial r^*}\right)+\frac{\partial\upsilon_r^2}{\partial z^2}-\varepsilon^2\frac{\upsilon_r}{(r^*)^2}\right] \quad (3)$$

Neglecting the terms ε and ε^2, which are very small, we have

$$-\rho\frac{r^*\omega^2}{\varepsilon}=\mu\frac{\partial\upsilon_r^2}{\partial z^2}. \quad (4)$$

Using the original coordinate in the radial direction with $r = \varepsilon^{-1}r*$, we have

$$\rho r\omega^2=-\mu\frac{\partial\upsilon_r^2}{\partial z^2}. \quad (5)$$

The left and right sides of Equation (5) correspond to the centrifugal and viscous forces, respectively, and are balanced along the r-direction [25], [26]. Equation (5) is integrated by employing the following boundary conditions.

(i) No-slip conditions on the wafer surface.

$$\upsilon_r = 0 \quad at\ z = 0. \quad (6)$$

(ii) Free surface condition at the interface between the color PR and vacuum, where the shear force disappears.

$$\frac{\partial\upsilon_r}{\partial z} = 0 \quad at\ z = h, \quad (7)$$

where h is the height of the color PR coated on the wafer. Integrating Equation (5) twice (the balance between the centrifugal and viscous forces) and using boundary conditions (6) and (7) yields

$$\upsilon_r=\frac{\rho r\omega^2h^2}{\mu}\left[\frac{z}{h}-\frac{z^2}{2h^2}\right]. \quad (8)$$

Equation (8) describes the radial velocity with respect to film height h. Using Equation (8), the radial flow of color PR per unit length of the circumference is given by

$$q = \int_0^h \upsilon_r dz = \frac{\rho r \omega^2 h^3}{3\mu}. \quad (9)$$

The continuity equation in the radial direction is

$$\frac{\partial h}{\partial t} + \frac{1}{r}\frac{\partial}{\partial r}(rq) = 0. \quad (10)$$

Substituting Equation (9) into Equation (10) yields

$$\frac{\partial h}{\partial t} + \frac{2\rho\omega^2 h^3}{3\mu} = 0. \quad (11)$$

Solving Equation (11) with $h\,(t = 0) = h_0$, where h_0 is the initial height of the fluid, we obtain

$$h = \frac{h_0}{\left(1 + \frac{4\rho\omega^2}{3\mu} h_0^2 t\right)^{1/2}}. \quad (12)$$

Assuming $4\rho\omega^2 h_0^2 t / 3\mu \gg 1$, we obtain

$$h = \sqrt{\left({}^{3\mu}\!/_{4\rho t\omega^2}\right)}. \quad (13)$$

Equation (13) indicates that the variation in the film height (h) of the color PR can be controlled by the viscosity (μ), coating process time (t), and angular velocity (ω).

IV. INVESTIGATION OF THE DIAGONAL STRIATION PATTERN

Diagonal patterns were investigated to determine the parameters that control these patterns. As shown in the left panel of Fig. 3(a), a clear diagonal discoloration was found to be consistent with the pad pitch upon inspection with an optical scope because the bump pads act as coating barriers. Moreover, they interfere with the PR flow, creating a wide and long turbulent wake behind the pads. We introduced the "flow past a sphere" theory [27] of fluid dynamics in the spin-coating process to determine the control parameters of the wake width. According to the theory, the drag force for a sphere is a function of the Reynolds number (Re) [28]. The drag force (F_D) is the resistance force acting in the direction opposite to the relative flow velocity between the body and fluid. The drag coefficient (C_D) is a dimensionless quantity used to quantify F_D in a fluid environment. F_D is given by

$$F_D = \frac{1}{2}\rho\upsilon^2 C_D A, \quad (14)$$

where υ is the velocity of the fluid, and A is the cross-sectional area of a sphere. The value of C_D depends on the shape of the object and Re, which is the ratio of the inertial and viscous forces within a fluid and is given by

$$Re = \frac{\upsilon D}{\boldsymbol{\nu}} = \frac{\rho\upsilon D}{\boldsymbol{\mu}} \quad (15)$$

where $\boldsymbol{\nu}$ is the kinematic viscosity (μ/ρ) of the fluid, and D is the equivalent diameter of the object. The relationship between Re and C_D is similar to that shown in the bottom panel of Fig. 3(b). When $Re < 1$ (Stage 1), the inertial forces are negligible, and viscous forces become dominant. Owing to the full viscous effect, the streamline is attached symmetrically to the wall of the sphere [29]. As Re increases to 40 (Stage 1 → 2), a wake with a recirculation zone is developed behind the sphere owing to the contribution of inertial forces. When Re increases to 100 (Stage 2 → 3), alternating vortices are triggered by the small perturbations behind the sphere, which is known as the vortex shedding phenomenon [30]. When Re is in the range of 400 to 3×10^5 (Stage 4), the laminar boundary separation phenomenon occurs, in which the streamlines separate from the surface. In this region, the separation angle is less than 90°, resulting in a wide wake referred to as subcritical flow [31]. For $Re \approx 3 \times 10^5$ (Stage 5), the boundary layer of the fluid changes from laminar to turbulent flow immediately after passing through the separation points with a 90° separation angle. At the abrupt transition, there is critical flow that supplies energy to the boundary layer detached from the laminar separation points, forming additional turbulent separation points behind the sphere. The reattaching property of the turbulent layer results in the formation of a narrow wake, and C_D suddenly decreases. This is known as a drag crisis [32]–[34]. As Re further increases (Stage 5 → 6), the laminar separation points merge with the turbulent separation points on the reverse side of the sphere with a separation angle greater than 90°, further reducing the wake width. Considering the spin coating RPM and viscosity of color PR, the range of Re belongs to Stage 5, where a wide wake width is inevitable. These investigations indicated that the coating process had to be optimized by further increasing Re (Stage 4 → 6) to narrow the wake width of the diagonal patterns.

V. CFD SIMULATION EXPERIMENTS

As shown in Fig. 4(a), the layout geometry was created by reflecting the actual dimensions using SolidWorks software [35]. The geometry was imported into the ICEM-CFD [36] to generate a mesh structure. The minimum element size of the mesh was 0.1 mm and was optimized to reduce the total computing time. The structured mesh was also imported into the Fluent Ansys solver [37] to calculate the mass, momentum, and energy conservation equations. Finally, the CFD simulation was conducted by rotating the geometry based on the real spin-coating parameters, such as the wafer rotation speed, process time, and viscosity of the PR. The CFD simulation results successively demonstrated the striation pattern identified in the in-line inspection results in terms of each position. Points 1 and 3, which represent the corners at 12 and 3 o'clock, respectively, showed an orthogonal stripe pattern. Point 2, representing 1 o'clock, showed a diagonal pattern.

From Equations (13) and (15), ω, t, D, and μ were identified as the key parameters that would need to be adjusted to reduce the diagonal and orthogonal patterns. Among

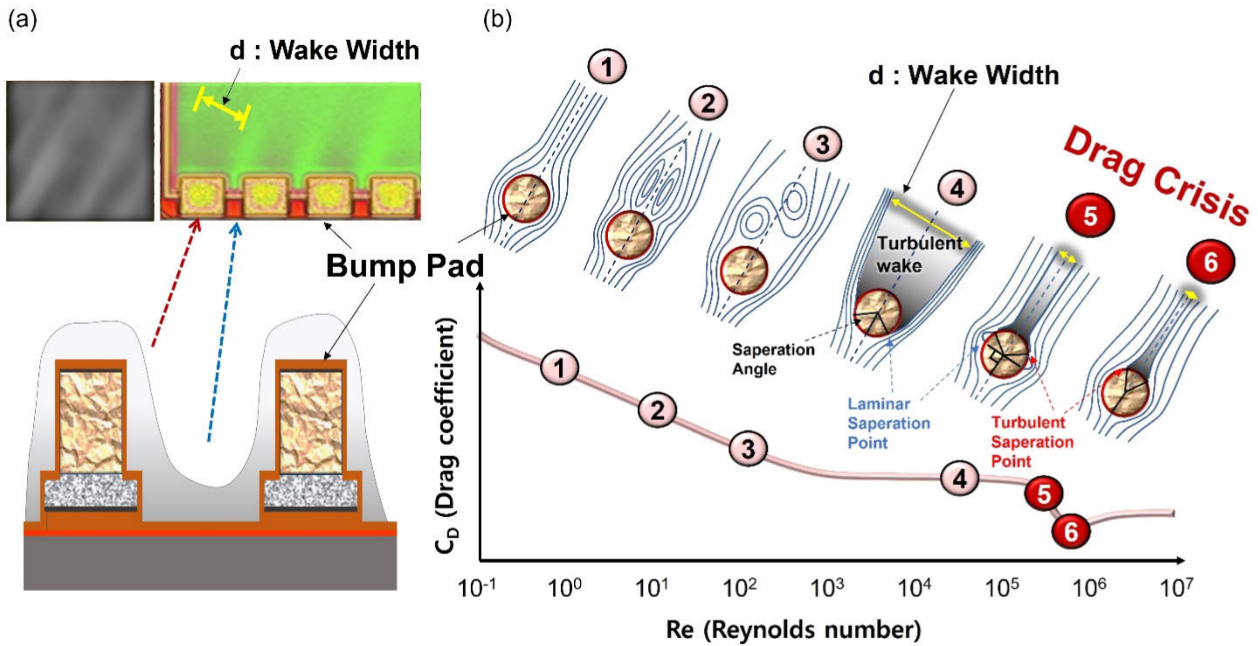

FIGURE 3. Graphical description of diagonal striation pattern: (a) inspection results near bump pad area and the corresponding vertical cross-section schematic, (b) fluid streamline past a sphere and the relationship between drag coefficient and Reynolds number. At Stage 1, the streamline is attached symmetrically to the wall of the sphere. Stage 1 → 2, a wake with a recirculation zone is developed behind the sphere. Stage 2 → 3, alternating vortices are triggered behind the sphere. Stage 4, the laminar boundary separation phenomenon occurs. Stage 5, the boundary layer of the fluid changes from laminar to turbulent flow. Stage 5 → 6, the laminar separation points merge with the turbulent separation points at the backside of the sphere.

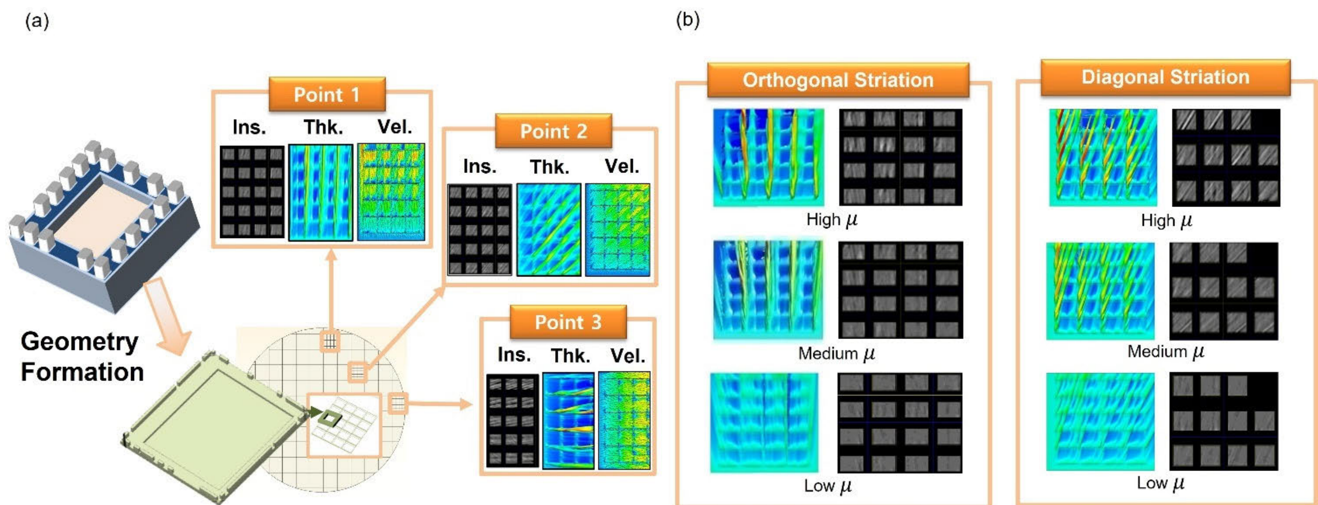

FIGURE 4. Experiment and evaluation with the CFD simulation: (a) inspection images versus simulation results in terms of the wafer location — Ins.: inspection; Thk.: thickness; Vel.: velocity, (b) color PR viscosity experiment for orthogonal and diagonal striation patterns. Each test was performed with three different values of μ (high, medium, and low) and the other parameters were kept constant. The striation patterns in the orthogonal and diagonal directions were considerably less prominent when a color PR with lower μ was applied.

them, it was not possible to change the spin coating process parameters (ω and t) and bump pad diameter D because the required processing time would be too long and the pad size was standardized. Therefore, μ is the only common parameter that lends itself to simultaneously reducing the diagonal and orthogonal patterns. Color PR coating experiments were conducted by varying the value of μ in the CFD simulations and wafer-level tests. Each test was performed with three different values of μ (high, medium, and low) whereas other parameters, such as the coating process time and wafer rotation speed, were kept constant. As shown in Fig. 4(b), striation in the orthogonal and diagonal patterns was considerably less when a color PR with a lower μ was applied.

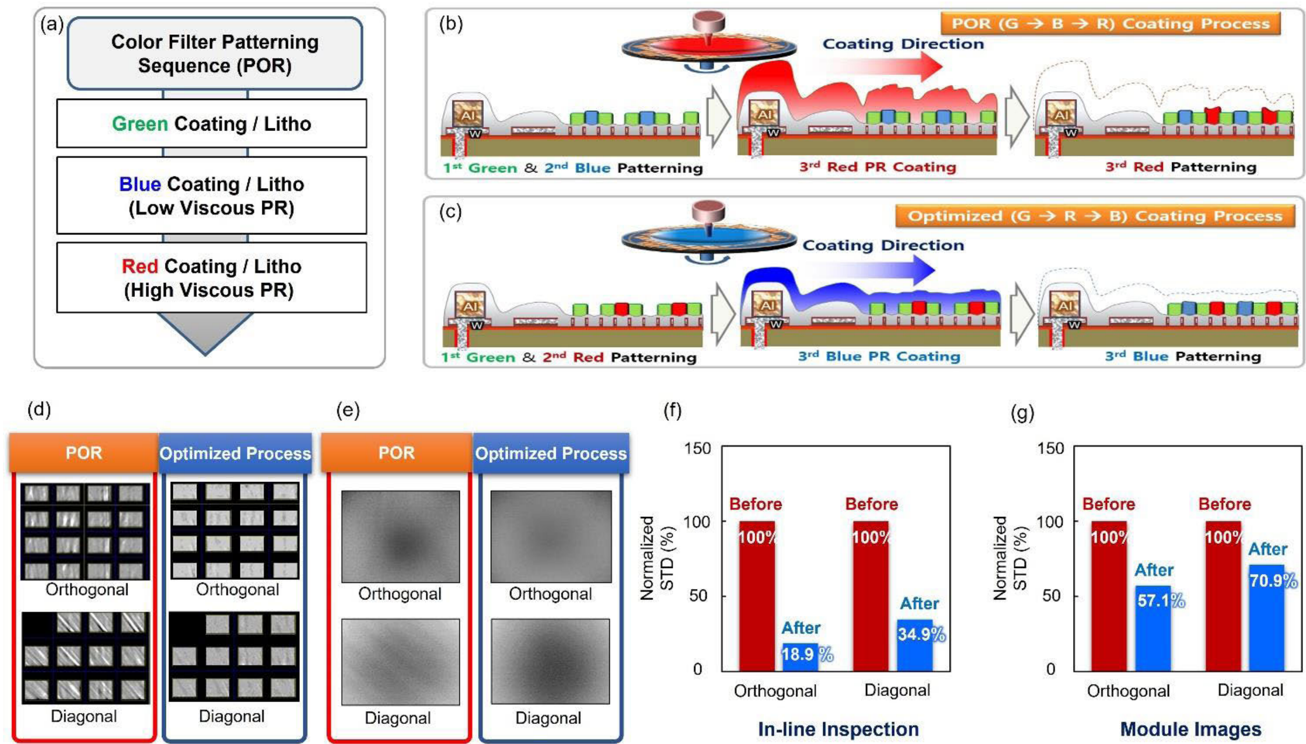

FIGURE 5. Rearrangement of the color PR coating order: (a) CF patterning sequence (POR), (b) graphical illustration of POR coating sequence, (c) graphical illustration of optimized coating sequence, (d) in-line data comparison between POR and optimized process, (e) image-capture data comparison between POR and optimized process, and normalized STD (%) comparison between the POR process and the optimized coating process from (f) in-line inspection and (g) module images.

VI. REARRANGEMENT OF THE COLOR PR COATING ORDER

We aimed to improve the overall color PR coating variation by examining the order in which the CFs of the different colors in the PR coating process were fabricated. As shown by the CF patterning order of the process of record (POR) in Fig. 5(a), the red CF, which has the highest viscosity among the three CF layers, was placed last in the sequence. The process to fabricate the last CF may always be imperfect because it has to take into account the step heights created previously by the other colors. When the red PR, which had the highest viscosity, spread unevenly on the textured surface, the uniformity of the shape and thickness in the created CF was degraded, resulting in poor striation patterns in the CF, as schematically shown in Fig. 5(b). To overcome this problem, the CF coating sequence was optimized by fabricating the blue CF, which had the lowest viscosity, at the end, as indicated in Fig. 5(c). The in-line inspection data in Fig. 5(d) show that both types of patterns improved remarkably after the optimized CF coating process was applied. In addition, the image sensors fabricated with the optimized CF coating order had excellent optical uniformity, even under enhanced image test conditions at the module level, as shown in Fig. 5(e). Finally, we quantitatively confirmed the improvement of the optimized coating process compared to the POR process with the normalized standard deviation (STD) in Fig. 5(f) and (g). Based on the in-line inspection results, the normalized STD was improved by 81.1% (100% to 18.9%) for the orthogonal pattern and 65.1% (100% to 34.9%) for the diagonal pattern. Moreover, the enhanced image test at the module level showed an improvement of 42.9% (100% to 57.1%) for the orthogonal pattern and 29.1% (100% to 70.9%) for the diagonal pattern.

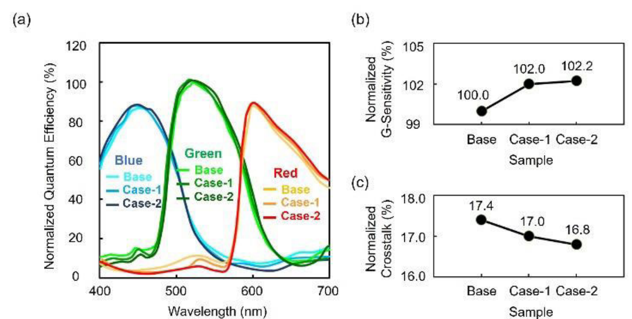

FIGURE 6. Comparison of the normalized quantum efficiency: (a) spectral responses of the red, green, and blue CF arrays with respect to each process condition (Base: unoptimized condition, Case-1: low viscosity condition, Case-2: low viscosity & process re-arrangement), (b) normalized G-sensitivity (%), and (c) normalized crosstalk (%).

Finally, after fine-tuning the thickness and CD of the color layers, the spectral responses of the red, green, and blue CF arrays were compared with respect to each process condition, as shown in Fig. 6(a). (Base: unoptimized

condition, Case-1: low viscosity condition, Case-2: low viscosity and process rearrangement). Notably, the normalized sensitivity and crosstalk of Case-2 was improved from 100% to 102.2% and from 17.4 % to 16.8%, respectively, compared to the base condition, as shown in Fig. 6(b) and (c). The improved crosstalk level is quite close to that of the most recently reported state-of-the-art CMOS image sensors (15.0–16.3 %) [38]–[40].

VII. CONCLUSION

The 3D coating process of a CF resist that induced various radial-shaped striation patterns was studied thoroughly. The CF fabrication process was found to have highly uniform optical properties in the CIS manufacturing process. The 3D radial-shaped striation patterns were categorized into two types: the orthogonal type, found only at the orthogonal edges of the wafer, and the diagonal type, which is mainly found at each quadrant edge. The orthogonal pattern was found to be caused by the wide standing wave created by the incident force of the spreading PR and the reflective force from the bump pads. The diagonal pattern was generated by the turbulent wakes created behind the bump pads owing to the drag force that interferes with the coating flow. An in-depth study using CFD simulations and in-line experiments confirmed that lowering the viscosity of each color PR was the most effective way to address both the orthogonal and diagonal types of striation. Consequently, by decreasing the viscosity values of each color PR, the 3D striation patterns improved drastically. This study elucidates the coating mechanism of the CF process in CIS mass production.

ACKNOWLEDGMENT

The authors would like to express their deepest gratitude to Dr. J. H. Ku and Dr. Y. K. Hong of Samsung Foundry Division for their insightful comments and support for this research. They also thank S. I. Jung of the Samsung Foundry Division, who provided academic support.

REFERENCES

[1] J. Ahn, K. Lee, Y. Kim, H. Jeong, B. Kim, H. Kim, J. Park, T. Jung, W. Park, and T. Lee, "7.1 A 1/4-inch 8 mpixel CMOS image sensor with 3D backside-illuminated 1.12 μm pixel with front-side deep-trench isolation and vertical transfer gate," in *Proc. IEEE Int. Electron Devices Meet.*, Feb. 2014, pp. 124–125.

[2] Y. Kim, W. Choi, D. Park, H. Jeoung, B. Kim, Y. Oh, S. Oh, B. Park, E. Kim, and Y. Lee, "A 1/2.8-inch 24 mpixel CMOS image sensor with 0.9 μm unit pixels separated by full-depth deep-trench isolation," in *IEEE Int. Solid-State Circuits Conf. (ISSCC) Dig. Tech. Papers*, Feb. 2017, pp. 84–86.

[3] J. Ohta, *Smart CMOS Image Sensors and Applications*. Boca Raton, FL, USA: CRC Press, 2020.

[4] I. Takayanagi and J. Nakamura, "High-resolution CMOS video image sensors," *Proc. IEEE*, vol. 101, no. 1, pp. 61–73, Jan. 2013.

[5] R. Lukac and K. N. Plataniotis, "Color filter arrays: Design and performance analysis," *IEEE Trans. Consum. Electron.*, vol. 51, no. 4, pp. 1260–1267, Nov. 2005.

[6] T. Sugiura, "Dyeing color-filters for liquid crystal display," *J. Soc. Inf. Display*, vol. 4, pp. 81–84, Jun. 1993.

[7] C. Sakong, Y. D. Kim, J.-H. Choi, C. Yoon, and J. P. Kim, "The synthesis of thermally-stable red dyes for LCD color filters and analysis of their aggregation and spectral properties," *Dyes Pigments*, vol. 88, no. 2, pp. 166–173, Feb. 2011.

[8] R. J. Lee, J. C. Fan, T. S. Cheng, and J. L. Wu, "Pigment-dispersed color resist with high resolution for advanced color filter application," *ITE Tech. Rep.*, vol. 98, no. 666, pp. 193–197, 1999.

[9] J. Park, Y. Park, and J. Park, "Synthesis and physical property measurement of new red pigment based on anthraquinone derivatives for color filter pigments," *Mol. Crystals Liquid Crystals*, vol. 551, no. 1, pp. 116–122, Nov. 2011.

[10] J.-P. Lu, F.-C. Chen, and Y.-Z. Lee, "Ring-edged bank array made by inkjet printing for color filters," *J. Display Technol.*, vol. 5, no. 5, pp. 162–165, May 2009.

[11] H.-S. Koo, P.-C. Pan, T. Kawai, M. Chen, F.-M. Wu, Y.-T. Liu, and S.-J. Chang, "Physical chromaticity of colorant resist of color filter prepared by inkjet printing technology," *Appl. Phys. Lett.*, vol. 88, no. 11, Mar. 2006, Art. no. 111908.

[12] T. Suzuki, C. Yoshikawa, T. Watanabe, and S. Wakeshima, "Development and industrialization of LCD color filters by electrodeposition method: Denchakuho ni yoru ekisho hyojiyo color filter no kaihatsu to kogyoka," *Nippon Kagaku Kaishi*, vol. 289, pp. 8–15, Jan. 1996.

[13] C. Sung, J. Han, J. Song, C. S. Ah, S. M. Cho, and T. Kim, "Reflective-type transparent/colored mirror switchable device using reversible electrodeposition with Fabry–Perot interferometer," *Adv. Mater. Technol.*, vol. 5, no. 10, Oct. 2020, Art. no. 2000367.

[14] H. Taguchi and M. Enokido, "Technology of color filter materials for image sensor," *Red*, vol. 10502, no. 8892, p. 3216, 2017.

[15] F. J. Maile, G. Pfaff, and P. Reynders, "Effect pigments-past, present and future," *Prog. Organic Coatings*, vol. 54, no. 3, pp. 150–163, 2005.

[16] D. Jang, D. Park, S. Cha, H. Kwon, M. Kim, S. Lee, H. Lee, S. Kim, N. Lee, and J. Han, "0.8μm-pitch CMOS image sensor with dual conversion gain pixel for mobile applications," in *Proc. Int. Image Sensor Workshop*, 2019, pp. 1–3.

[17] Y. Jang, H. Kim, K. Kim, S. Kim, S. Lee, and J. Yim, "A new PDAF correction method of CMOS image sensor with nonacell and super PD to improve image quality in binning mode," *Electron. Imag.*, vol. 2021, no. 9, pp. 220-1–220-5, 2021.

[18] D. Park, S.-W. Lee, J. Han, D. Jang, H. Kwon, S. Cha, M. Kim, H. Lee, S. Suh, and W. Joo, "A 0.8μm smart dual conversion gain pixel for 64 megapixels CMOS image sensor with 12 ke-full-well capacitance and low dark noise," in *IEDM Tech. Dig.*, Apr. 2019, pp. 16.2.1–16.2.4.

[19] I. S. Joe, Y. Lee, H. Y. Park, J. U. Kim, and D. Kang, "Development of advanced inter-color-filter grid on sub-micron-pixel CMOS image sensor for mobile cameras with high sensitivity and high resolution," in *Proc. Symp. VLSI Circuits*, Jun. 2021, pp. 1–2.

[20] C. Huang and Z. Wang, "Planarization of high topography surfaces with deep holes and cavities using two-step polymer coating," *Sens. Actuators A, Phys.*, vol. 213, pp. 94–101, Jul. 2014.

[21] Y. Yan, Y. Ding, T. Fukushima, K.-W. Lee, and M. Koyanagi, "Study of vacuum-assisted spin coating of polymer liner for high-aspect-ratio through-silicon-via applications," *IEEE Trans. Compon., Packag., Manuf. Technol.*, vol. 6, no. 4, pp. 501–509, Apr. 2016.

[22] H. S. Santana, A. G. P. da Silva, M. G. M. Lopes, A. C. Rodrigues, O. P. Taranto, and J. L. Silva, "Computational methodology for the development of microdevices and microreactors with ANSYS CFX," *MethodsX*, vol. 7, pp. 82–103, Jun. 2020.

[23] L. W. Schwartz and R. V. Roy, "Theoretical and numerical results for spin coating of viscous liquids," *Phys. Fluids*, vol. 16, no. 3, pp. 569–584, Mar. 2004.

[24] T.-S. Kim and M.-U. Kim, "The flow and hydrodynamic stability of a liquid film on a rotating disc," *Fluid Dyn. Res.*, vol. 41, no. 3, Jun. 2009, Art. no. 035504.

[25] A. G. Emslie, F. T. Bonner, and L. G. Peck, "Flow of a viscous liquid on a rotating disk," *J. Appl. Phys.*, vol. 29, no. 5, pp. 858–862, May 1958.

[26] N. Sahu, B. Parija, and S. Panigrahi, "Fundamental understanding and modeling of spin coating process: A review," *Indian J. Phys.*, vol. 83, no. 4, pp. 493–502, Apr. 2009.

[27] R. Turton and O. Levenspiel, "A short note on the drag correlation for spheres," *Powder Technol.*, vol. 47, no. 1, pp. 83–86, Mar. 1986.

[28] V. M. Vassilev, T. Kotsev, S. G. Nikolov, M. D. Datcheva, and Y. P. Ivanova, "Viscous flow around spherical particles in different arrangements," in *Proc. MATEC Web Conf.*, vol. 145, 2018, pp. 1–8.

[29] K. D. Housiadas, G. C. Georgiou, and R. I. Tanner, "A note on the unbounded creeping flow past a sphere for Newtonian fluids with pressure-dependent viscosity," *Int. J. Eng. Sci.*, vol. 86, pp. 1–9, Jan. 2015.

[30] A. Desai, S. Mittal, and S. Mittal, "Experimental investigation of vortex shedding past a circular cylinder in the high subcritical regime," *Phys. Fluids*, vol. 32, no. 1, Jan. 2020, Art. no. 014105.
[31] J. Hoffman, "Adaptive simulation of the subcritical flow past a sphere," *J. Fluid Mech.*, vol. 568, pp. 77–88, Dec. 2006.
[32] M. Geier, A. Pasquali, and M. Schönherr, "Parametrization of the cumulant lattice Boltzmann method for fourth order accurate diffusion Part II: Application to flow around a sphere at drag crisis," *J. Comput. Phys.*, vol. 348, pp. 889–898, Nov. 2017.
[33] S. P. Singh and S. Mittal, "Flow past a cylinder: Shear layer instability and drag crisis," *Int. J. Numer. Methods Fluids*, vol. 47, no. 1, pp. 75–98, Jan. 2005.
[34] P. Wen and W. Qiu, "Investigation of drag crisis phenomenon using CFD methods," *Appl. Ocean Res.*, vol. 67, pp. 306–321, Sep. 2017.
[35] D. S. SolidWorks, W. Street, and M. Waltham. *SOLIDWORKS 2016*. Accessed: Mar. 20, 2015. [Online]. Available: https://help.solidworks.com/
[36] I. Ansys, *CFD Tutorial Manual*, vol. 14. Canonsburg, PA, ISA: ANSYS, 2007.
[37] J. Matsson, *An Introduction to ANSYS Fluent 2020*. Tirupati, India: SDC, 2020.
[38] E. S. Shim, K. Lee, J. Pyo, W. Choi, J. Yun, T. Jung, K. Lee, S. Kim, C. Lee, S. Baek, H. Kim, S. Choi, J. Yang, K. Son, J. Choi, H. Park, B. Kim, J. Ahn, and D. Chang, "All-directional dual pixel auto focus technology in CMOS image sensors," in *Proc. Symp. VLSI Circuits*, Jun. 2021, pp. 1–2.
[39] Y. Oh, M. Kim, W. Choi, H. Choi, H. Jeon, J. Seok, Y. Choi, J. Jung, K. Yoo, and D. Park, "A 0.8 μm nonacell for 108 megapixels CMOS image sensor with FD-shared dual conversion gain and 18,000e full-well capacitance," in *IEDM Tech. Dig.*, Oct. 2020, pp. 16.2.1–16.2. 4.
[40] Y. J. Jung, V. C. Venezia, S. Lee, C. Y. Ai, Y. Zhu, K. W. Yeung, G. Park, W. Choi, Z. Lin, and W.-Z. Yang, "A 64 M CMOS image sensor using 0.7 μm pixel with high FWC and switchable conversion gain," in *IEDM Tech. Dig.*, May 2020, pp. 16.3.1–16.3.4.

SUNGJUN KIM (Member, IEEE) received the M.S. degree from the Department of Electrical and Computer Engineering, Sungkyunkwan University, South Korea, in 2013, where he is currently pursuing the Ph.D. degree. He is also employed as a Research and Development Engineer at Samsung Foundry. His current research interests include semiconductor process development for high-quality, reliable devices as well as analog synaptic devices with ferroelectric materials for neuromorphic application.

JAESANG YOO received the B.S. degree in materials science and engineering from Yonsei University, South Korea, in 2013. He is currently employed as a Research and Development Engineer at Samsung Foundry. His current research interests include CMOS image sensor technology and optoelectronic devices.

HAKYU CHOI received the M.S. degree in physics from Sungkyunkwan University, South Korea in 2007. He is currently a Research and Development Engineer at Samsung Foundry. His current research interests include semiconductor process development for high-quality and reliable devices.

JAEKWAN SEO received the B.S. degree in electronics engineering from Ulsan University, South Korea, in 2004. He is currently a Research and Development Engineer at Samsung Foundry. His current research interests include color-filter process development and process optimization.

SUNGHUN LEE received the B.S. degree in electrical engineering and electronic physics from Kwangwoon University, Seoul, South Korea, in 2017. He is currently pursuing the M.S. degree in advanced semiconductor devices with Sungkyunkwan University, Suwon, South Korea.

SANG MIN WON received the B.S., M.S., and Ph.D. degrees in electrical and computer engineering from the University of Illinois at Urbana Champaign. He is currently an Assistant Professor with the Department of Electrical and Computer Engineering, Sungkyunkwan University. His current research interests include sensors/stimulators with unique applications in advanced biomedical and/or health monitoring systems.

JIN-HONG PARK (Member, IEEE) received the M.S. and Ph.D. degrees in electrical engineering from Stanford University, USA, in 2006 and 2009, respectively. From 2009 to 2011, he was with Kyung Hee University, South Korea, and the IBM Thomas J. Watson Research Center, Yorktown Heights, NY, USA. Since 2011, he has been a Professor with the School of Electronic and Electrical Engineering and SKKU Advanced Institute of Nano Technology (SAINT), Sungkyunkwan University, South Korea. His current research interests include next-generation low-power devices based on 2D vdW materials (gate-all-around FETs, multi-valued logic devices, and neuromorphic devices) and the fabrication process technologies of 2D vdW materials.

KEUN HEO (Member, IEEE) received the Ph.D. degree in electronics engineering from Korea University, Seoul, South Korea, in 2014. He is currently an Associate Professor with the Semiconductor Physics Research Center, School of Semiconductor and Chemical Engineering, Jeonbuk National University. His current research interests include modeling, simulation, and system-level application of next-generation devices based on quantum nanomaterials.